Check for updates

Advanced Energy Materials

ADVANCED ENERGY MATERIALS
www.advenergymat.de

RESEARCH ARTICLE

Hydrogen Bond-Mediated Molecule-Cation Passivation Pair for Efficient Perovskite Solar Cells

Yi Lu | Min Wang | Yi Suo | Hao Huang | Qiang Zhang | Zhineng Lan | Wenyuan Xiao | Yanling Chen | Guanzheng Zhang | Ya Wu | Peng Cui | Meicheng Li

State Key Laboratory of Alternate Electrical Power System With Renewable Energy Sources, School of New Energy, North China Electric Power University, Beijing, China

Correspondence: Hao Huang (hhuang@ncepu.edu.cn) | Peng Cui (cuipeng@ncepu.edu.cn) | Meicheng Li (mcli@ncepu.edu.cn)

Received: 12 January 2026 | **Revised:** 15 April 2026 | **Accepted:** 17 April 2026

Keywords: interface | passivation | perovskite solar cells | perovskite surface

ABSTRACT

Homogeneous and efficient surface passivation is crucial for achieving the high photovoltaic performance in perovskite solar cells (PSCs). In this work, we engineered a universal passivation strategy by constructing a hydrogen bond-mediated molecule-cation passivation pair for widely used ammonium cations (phenethylammonium (PEA^+), propane-1,3-diammonium (PDA^{2+}), (2-(cyclohex-1-en-1-yl) ethan-1-aminium ($CHEA^+$)). This strategy disperses the ammonium passivators by leveraging the hydrogen bond-mediated interactions between 4-amino-3,5-difluorobenzonitrile (AFBN) and ammonium cations, mitigating their disordered accumulation on the perovskite surface and enabling a laterally homogeneous passivation. Besides, the cyano moieties of AFBN interact with undercoordinated Pb^{2+}, complemented by the amino groups, which engage in hydrogen bonding with I^- sites, delivering effective passivation of multiple defects through combining the traditional ammonium salt. Consequently, the p-i-n devices treated with AFBN/PEACl and AFBN/$PDAI_2$ achieved remarkable power conversion efficiencies (PCEs) of 25.89% and 26.77%, respectively. Furthermore, the AFBN/CHEAI pair enabled a high efficiency of 25.88% in n-i-p PSC. Moreover, the unencapsulated HMPP-PSCs also exhibit an enhanced device stability, maintaining 91.5% and 87.5% of their initial efficiencies after nearly 2500 h of aging in ambient air and heat soaking at 65°C for 800 h.

1 | Introduction

Perovskite solar cells (PSCs) have witnessed rapid advancements in recent years, driven by their compatibility with tandem devices, low-temperature fabrication process, and enhanced environmental stability, with power conversion efficiency (PCE) exceeding 27%. However, kinetic imbalance during solution-phase crystallization, coupled with lattice termination effects, often result in a high density of surface defects in the as-prepared films. In inverted PSCs, this challenge is further exacerbated by the weak interfacial interaction between the widely used electron transport layer (ETL), C_{60}, and the perovskite lattice, an issue that facilitates the formation of additional interfacial defects [1–7]. Consequently, developing effective and uniform surface passivation strategies is crucial to suppressing defect-mediated recombination and optimizing charge carrier transport, thereby improving the overall device performance [8, 9].

Ammonium cations/salts, such as phenethylammonium chloride (PEACl), propane-1,3-diaminium iodide ($PDAI_2$), 2-(cyclohex-1-en-1-yl) ethan-1-aminium iodide (CHEAI), phenethylamine hydroiodide (PEAI), butylamine hydroiodide (BAI), have been widely employed to passivate surface defects of perovskite films [10–12]. In most cases, the ammonium cation occupies the voids within the Pb–I framework to passivate formamidinium

© 2026 Wiley-VCH GmbH

(FA) vacancies. However, individual passivators typically suffer from an intrinsic limitation in neutralizing diverse defects; for instance, ammonium salts exhibit a lack of efficacy against under coordinated Pb^{2+} and I^- sites [13–15]. To broaden the functional scope, composite passivation systems are frequently employed. More critically, as documented in recent literature, ammonium cations are prone to non-uniform surface distribution [16–19]. Merely stacking multiple functional groups within a composite system often fails to achieve the desired homogeneity; instead, the increased molecular complexity may exacerbate the uneven distribution, ultimately leading to negative effects on device performance [17, 20]. In fact, to address the limitations of single-component passivators and the issue of non-uniform passivation, numerous studies have explored alternative strategies, such as dual-site passivation and synergistic dual-molecule passivation, to achieve more effective defect passivation and improved device performance. Chen et al. [21] introduced a passivating molecule, 4-chlorobenzenesulfonate, which adopts a parallel orientation on the perovskite surface. Its dual active sites effectively enhance the passivation performance. Liu et al. [22] employed two surface passivation molecules with distinct functionalities: one achieves chemical passivation through coordination and hydrogen bonding, while the other utilizes field-effect passivation to suppress interfacial recombination, thereby maximizing interfacial quality. Cai et al. [23] introduced 3-ammonium bromide to achieve complementary passivation with phenethylammonium bromide, aiming to reduce the defect density arising from I and FA vacancies. Chen et al. [24] simultaneously incorporated a bulk passivator and a surface modifier, achieving both bulk and surface passivation, while utilizing hydrogen-bond interactions to induce the uniform distribution of the modifier along surface grain boundaries. Although extensive studies have focused on complementary passivation strategies, research that effectively reconciles the enhancement of passivation efficacy with the full-area uniformity of the passivator remains notably scarce.

We proposed a hydrogen bond-mediated molecule-cation passivation pair (HMPP) strategy to synergistically boost passivation efficacy and ensure long-range surface uniformity. Considering the suitable functional groups (cyano, amino (—NH_2)) and rigid planar molecular structure, the 4-amino-3,5-difluorobenzonitrile (AFBN) was selected after rational design and experiment (Figure S1) to construct the molecule-cation passivation pair. By integrating AFBN with traditional ammonium salts (e.g., PEACl and $PDAI_2$), we developed a molecular-cation passivation pair that achieves multifunctional composite passivation while effectively suppressing the inherent aggregation of ammonium cations. Using this strategy, we first constructed a passivation pair of PEA^+-AFBN, boosting the PCE from 24.20% to 25.89%. Furthermore, the HMPP strategy can also be performed to construct a PDA^{2+}-AFBN, delivering an overall efficiency enhancement with the champion PCE of 26.77%. This strategy can also be well applied in regular PSCs with the passivators of CHEAI, demonstrating the reliable universality. In addition, this strategy also enhances the device storage stability due to its effective passivation ability on various types of defects.

2 | Results and Discussion

2.1 | Molecule-Cation Passivation Pair Interactions

The PEACl, a passivator normally used in PSCs, was utilized as the surface passivator, and the AFBN was designed to construct a pair with PEA^+, leading to a uniform and effective surface passivation. The molecular structures and electrostatic potential (ESP) maps of PEACl and AFBN are shown in Figure 1a. Compared to the 4.37 Debye dipole moment of PEACl, AFBN possesses a larger dipole moment of 7.17 Debye. This dipole is highly directional, with negligible contributions along the y and z axes. It is reported that the ammonium cations like PEA^+ exhibit local aggregation, which causes the ineffective passivation and uneven charge distribution across the film [19, 25, 26]. Our strategy is to preassemble AFBN and PEACl into a complementary passivation pair, the hydrogen bond-mediated molecule-cation passivation pair. To verify this hypothesis, we first carried out density functional theory (DFT) calculations of the interaction for the PEACl dimer, the PEA^+-AFBN pair, and the AFBN dimer (Figure 1b). The results show that the binding energy of the PEA^+–AFBN pair is more negative than that of their respective dimers (−0.48 eV vs. −0.26 and −0.38 eV), suggesting that PEACl and AFBN can overcome self-attraction to form an aggregate theoretically. To experimentally explore the interaction between PEACl and AFBN, the measurements of ^1H nuclear magnetic resonance (NMR) spectroscopy and Fourier transform infrared (FTIR) spectroscopy were carried out. The ^1H NMR spectroscopy (Figure 1c) shows that the ammonium group (—NH_3^+) of PEA^+ exhibited an upfield shift (8.24–8.2 ppm) and the —NH_2 of AFBN experienced a slight downfield shift (6.35–6.37 ppm) in the mixture. This indicates the formation of a hydrogen bond between the two components, where the —NH_2 group acts as a hydrogen-bond acceptor, leading to the deshielding of its protons. The observed upfield shift (decreased δ value) of —NH_3^+ (as the hydrogen-bond donor) likely stems from the incorporation of AFBN, which disrupts the original strong deshielding environment of the —NH_3^+ cations mainly from the solvent, resulting in a relatively slight increase in electron density (shielding effect) [27–31]. As illustrated in Figure 1d, upon mixing the powders, the PEACl peak at 1116 cm^{-1} exhibits a blue shift to 1120 cm^{-1}, indicative of modulated C—N stretching vibrations. Concurrently, the AFBN peak at 1609 cm^{-1}, assigned to the coupling of aromatic skeletal and N-H bending vibration mode, shifts to 1603 cm^{-1}. Collectively, these synchronized spectral shifts corroborate the formed hydrogen bond discussed in ^1H NMR results [32–34]. This formed PEA^+-AFBN pair may mitigate the disordered aggregation of PEA^+ passivators on the perovskite surface.

Considering that the AFBN shows a large dipole, the AFBN is expected to passivate undercoordinated Pb^{2+} defects through the N—Pb bond. The X-ray photoelectron spectroscopy (XPS) measurement was carried out on perovskite films passivated by PEACl and the molecule-cation passivation pair, respectively. Notably, in the following discussion, the perovskite film and corresponding device after passivation with molecule-cation passivation pair were labelled as HMPP-sample, and the

16146840, 2026, 28, Downloaded from https://advanced.onlinelibrary.wiley.com/doi/10.1002/aenm.71112 by North China Electric Power University Beijing, Wiley Online Library on [05/09/2026]. See the Terms and Conditions (https://onlinelibrary.wiley.com/terms-and-conditions) on Wiley Online Library for rules of use; OA articles are governed by the applicable Creative Commons License

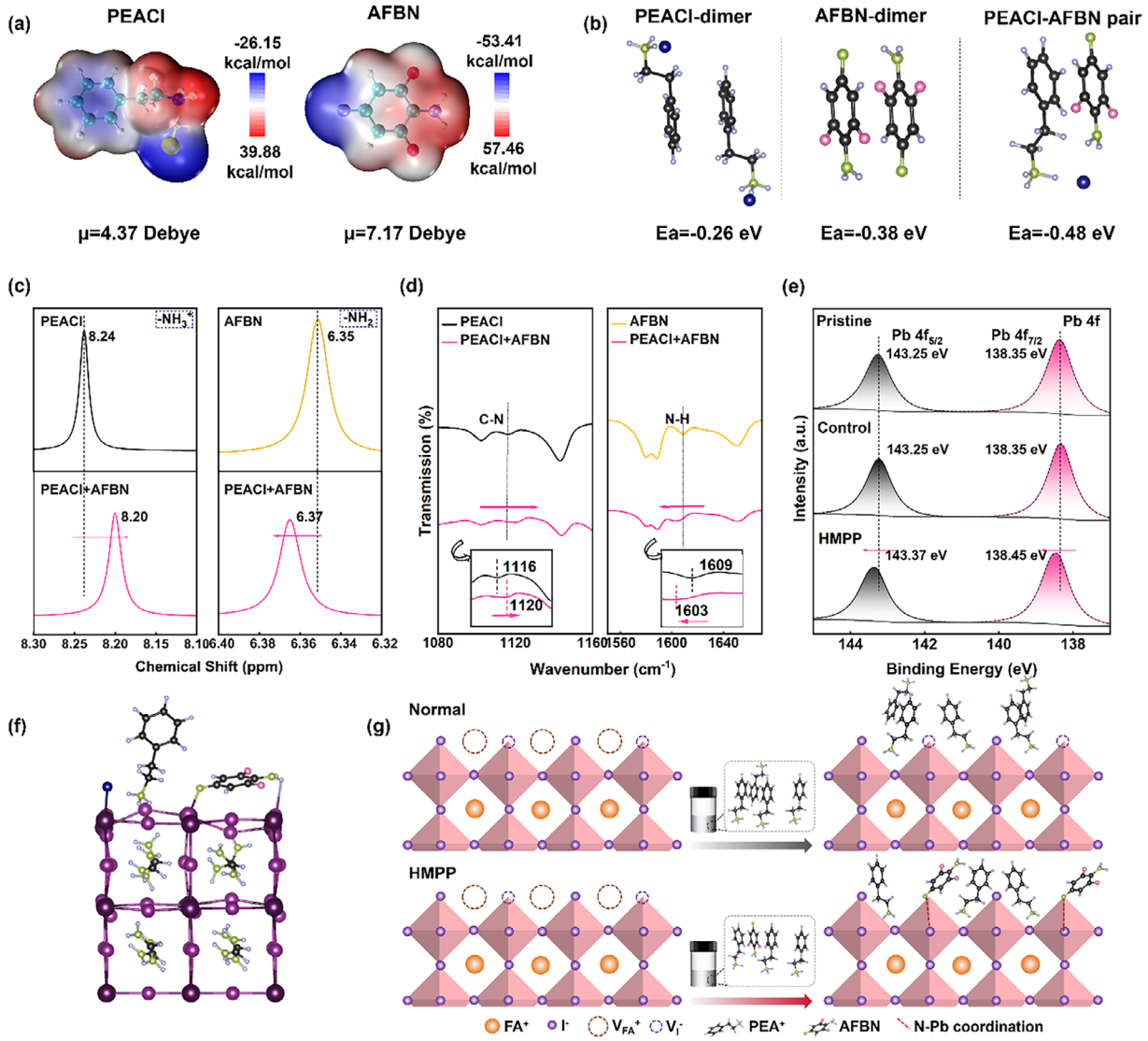


FIGURE 1 | The construction of a hydrogen bond-mediated molecule-cation passivation pair. (a) Molecular and ESP distribution of PEACl and AFBN. (b) The binding energies of the PEACl dimer, AFBN dimer, and the PEACl–AFBN pair. (c) ^{1}H NMR spectra of PEACl, AFBN, and PEACl mixed with AFBN. (d) FTIR spectra of PEACl powder, AFBN powder, and the PEACl–AFBN mixed powder. (e) XPS spectra of Pb 4f in prisitine, control and HMPP perovskite films. (f) The optimized PEACl-vertical and AFBN-parallel configuration. (g) Schematic of the PEACl–AFBN passivation pair interacting with perovskite surface atoms.

counterparts were labeled as control sample. In the XPS results, the binding energies of the Pb 4f remain nearly unchanged after the deposition of PEACl alone (Figure 1e). The absence of a noticeable binding energy shift in the main Pb 4f peaks is possibly because the chloride ions volatilized during the thermal annealing process (Figure S2). However, upon passivation with the molecule-cation passivation pair, both Pb 4f peaks shift to higher binding energies, indicating the interaction between Pb^{2+} and AFBN. Furthermore, the I 3d spectra of the HMPP film reveal a consistent shift of both I $3d_{3/2}$ and I $3d_{5/2}$ levels toward higher binding energy (Figure S3), which indicates that the amino group of AFBN partially interacts with iodide species [35–39]. The DFT calculation was further utilized to calculate the optimized configurations of PEACl and AFBN on the perovskite surface (Figure S4). Through a series of adsorption energy calculations and comparisons, we identified that the system reaches its energy minimum when the benzene ring of PEACl is oriented perpendicular to the perovskite surface, while AFBN remains parallel to the surface. This specific arrangement offers the probability for AFBN to simultaneously coordinate with both Pb^{2+} and I^{-} defect sites (Figure 1f). Additionally, the 3D charge density difference of the interfaces was calculated (Figure S5). The HMPP-modified interface displays a more coherent electron-accumulation region across the entire perovskite top-surface. This suggests that the HMPP strategy forms a more compact and uniform passivation layer. The proposed mechanism for the HMPP-mediated passivation strategy is depicted in Figure 1g.

2.2 | Enhanced Passivation Efficacy and Uniformity

After treating the perovskite surface with the PEA^{+}-AFBN passivation pair, we first examined the film morphology using

16146840, 2026, 28, Downloaded from https://advanced.onlinelibrary.wiley.com/doi/10.1002/aenm.71112 by North China Electric Power University Beijing, Wiley Online Library on [05/09/2026]. See the Terms and Conditions (https://onlinelibrary.wiley.com/terms-and-conditions) on Wiley Online Library for rules of use; OA articles are governed by the applicable Creative Commons License

scanning electron microscopy (SEM, Figure S6). The residual PbI_2 was slightly reduced upon the introduction of AFBN, indicating a modest improvement in passivation, which leads to a smoother and more compact film surface [40–42]. A similar conclusion was supported by the X-ray diffraction analysis (Figure S7), where the diffraction peak of PbI_2 at 12.6° decreased while the main diffraction peaks of the perovskite remained unchanged. The passivation layer on the perovskite surface for the HMPP-treated samples can be characterized by the cross-sectional transmission electron microscopy images (Figure S8).

Subsequently, to evaluate the enhanced passivation efficacy, we performed steady-state photoluminescence (PL) and space-charge-limited current (SCLC) measurements. We conducted PL measurement on perovskite films, which were fabricated on glass. The HMPP film exhibits a substantially increased PL intensity compared to the control film (Figure 2a), demonstrating the enhanced effectiveness of surface passivation, leading to reduced surface defect states. To quantitatively evaluate the defect density of the perovskite film, we fabricated electron-only devices and performed SCLC measurements (Figure 2b). The defect density can be calculated according to the equation of $Nt = 2\varepsilon\varepsilon_0 V_{TFL}/eL^2$. In this equation, ε is the relative dielectric constant, ε_0 the vacuum permittivity, e the electron charge, L the thickness of the perovskite film (Figure S9), and V_{TFL} the trap-filled limit voltage. As shown in Figure 2b, the V_{TFL} decreases from 0.14 V for the control device to 0.07 V for the HMPP device, corresponding to the defect density decreases from 1.48×10^{15} to 7.0×10^{14} cm^{-3}. This 50% reduction in trap density suggests significantly enhanced defect passivation, which is conducive to more efficient charge transport and a pronounced suppression of non-radiative recombination [43–45]. To gain deeper insights into the recombination kinetics and trap-mediated losses, we conducted light intensity-dependent photoluminescence quantum yield (PLQY) measurements to derive the quasi-Fermi level splitting (QFLS). Under 1-sun illumination, the PLQY values for the control and HMPP groups are 3.5% and 6.1% (Figure S10), with corresponding QFLS values of 1.167 and 1.179 eV (Figure 2c), respectively. This consistent enhancement in QFLS directly suggests a substantial reduction in the non-radiative recombination rate within the perovskite bulk or at its surfaces, resulting from the effective defect passivation by HMPP.

To further substantiate the passivation homogeneity and evaluate the passivation efficacy, we performed PLQY mapping. Figure 2d,e presents the PLQY mapping comparison between the control and HMPP films. In the control film, the red regions corresponding to relatively high PLQY appear as scattered spots, which may result from the local enrichment of PEA^+ on the perovskite surface. In contrast, the HMPP film exhibits a uniformly red distribution across the entire area, with higher PLQY values. These increased PLQY values and homogenized distribution demonstrate that the PEA^+-AFBN passivation pair results in a lower defect density and a more homogeneous suppression of non-radiative recombination [23, 46, 47]. Additionally, by monitoring the PLQY of each specimen before and after C_{60} deposition (Figure 2f), we systematically evaluated the interfacial landscapes established by PEACl-only passivation and by the HMPP-assisted passivation strategy. For the control sample, the PLQY decreases from 5.6% before deposition to 5.1% after C_{60} deposition, indicating severe interfacial non-radiative recombination. In contrast, the HMPP sample exhibits PLQY values of 6.7% and 6.6% before and after deposition, respectively. Compared with the sharp drop observed in the control, the slight reduction in the HMPP sample confirms that the PEACl–AFBN passivation pair effectively improves interfacial quality and suppresses non-radiative recombination [47–49]. We also conducted atomic force microscopy (AFM) measurement (Figure S11). The root-mean-square roughness of the film decreases from 18.26 nm for the control film to 15.56 nm for the HMPP film. The 2D height statistics histograms and height distribution extracted from the horizontal line profiles of AFM images (Figure S12) further corroborate the surface uniformity of the HMPP-treated sample. We additionally performed conductive atomic force microscopy measurements (Figure S13). The HMPP sample displays a significantly more homogeneous and continuous current distribution across the scanned area, with a higher average current (13.36 and 13.74 nA).

Correspondingly, the Kelvin probe force microscopy (KPFM) measurements reveal a much more pronounced improvement in surface potential uniformity with the PEA^+-AFBN passivation pair (Figure 2g–i). While the control film exhibits a heterogeneous contrast of bright and dark regions, the HMPP film shows a uniformly distributed and overall higher surface potential. This reduced heterogeneity of surface potential can also be validated by the 2D potential statistics histograms and potential distribution extracted from the horizontal line profiles (Figure 2i) more detailly, where the histogram shows a narrower range, and the extracted potential line shows a lower fluctuation. This improved uniformity of surface potential indicates a more homogeneous passivation with the PEA^+-AFBN pair, which in turn facilitates uniform carrier transport [50–52].

2.3 | Physical Property and Photovoltaic Performance of PSCs

We further conducted a range of electrical and optoelectronic measurements to gain deeper insights into the device physics and internal interfacial charge transport. We first performed ultraviolet photoelectron spectroscopy (UPS) on the perovskite films to investigate the effect of the HMPP strategy on the surface energetics and interfacial energy level alignment. As shown in Figure 3a, the secondary electron cutoff (E_{cutoff}) of the perovskite film shifted from 16.17 eV (control) to 16.10 eV (HMPP), corresponding to an increase in the work function from 5.05 to 5.12 eV. This slightly changed work function may stem from the relatively parallel configuration of AFBN. Combining the UPS spectra of the C_{60} film (Figure S14) and the optical band gaps extracted from the Tauc plots (Figure S15), the energy level alignment between the perovskite and C_{60} is illustrated in Figure 3b. The conduction band minimum (CBM) of the perovskite film aligns more closely with the CBM of C_{60}. This optimized energetic alignment maintains a sufficient driving force for electron extraction while effectively reducing carrier recombination by interfacial defects [21, 53]. We further conducted opto-electrical evaluations to experimentally verify these improved carrier dynamics. The time-resolved photoluminescence spectroscopy (TRPL) was carried out first on the single-layer perovskite films (pristine, control, and HMPP) to evaluate the intrinsic defect density (Figure S16 and Table S1). The results reveal a successive prolongation of average

16146840, 2026, 28, Downloaded from https://advanced.onlinelibrary.wiley.com/doi/10.1002/aenm.71112 by North China Electric Power University Beijing, Wiley Online Library on [05/09/2026]. See the Terms and Conditions (https://onlinelibrary.wiley.com/terms-and-conditions) on Wiley Online Library for rules of use; OA articles are governed by the applicable Creative Commons License

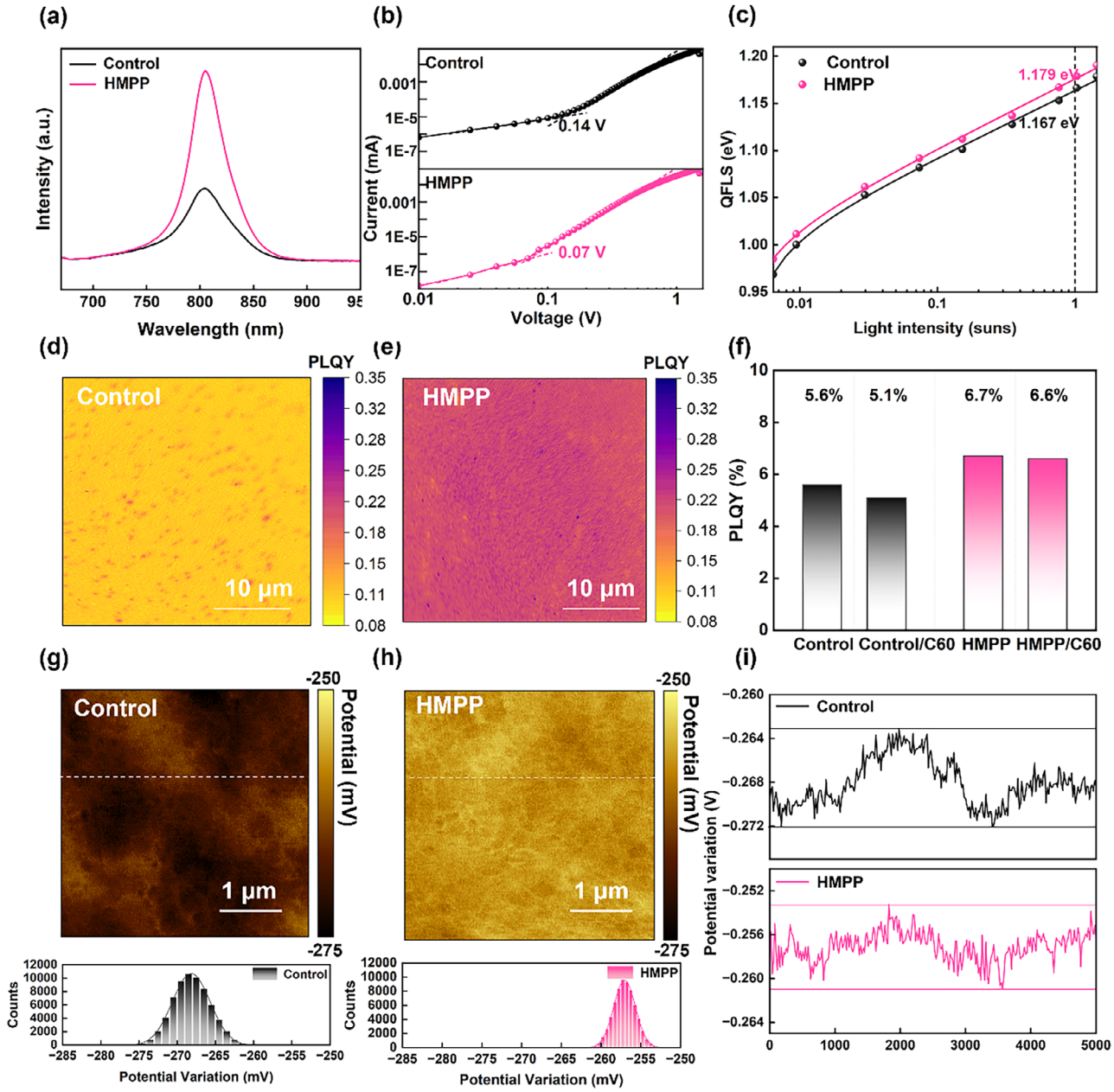


FIGURE 2 | The enhanced passivation efficacy and uniformity. (a) Steady-state PL spectra of the control and HMPP films deposited on glass. (b) SCLC curves of electron-only devices. (c) QFLS plot of control and HMPP perovskite films under illumination at different light intensities. PLQY mapping images of (d) control and (e) HMPP films. (f) PLQY values of the control and HMPP films before and after C_{60} deposition. (g, h) KPFM images of the control and HMPP films and (i) corresponding surface potential distribution.

carrier lifetimes ($\tau_{average}$) across these films. We also collected the TRPL data for the perovskite/C_{60} configuration and evaluated the carrier dynamics (Figure 3c; Table S1). Compared to the pristine and control films, the HMPP-treated film exhibits the shortest τ_1 (associated with interfacial charge transfer), the longest τ_2 (associated with radiative recombination in the bulk), and the highest $\tau_{average}$, indicating accelerated charge extraction alongside suppressed non-radiative recombination [54, 55]. The Mott–Schottky measurements revealed that the built-in electric field increased from 0.98 V for control PSCs to 1.02 V for HMPP PSCs (Figure 3d), which should result from the enhanced surface passivation and slightly optimized interfacial energy alignment [56, 57]. In addition, the photovoltage decay behavior, which mainly reveals the charge recombination process, was carried out (Figure S17), which shows the photovoltage decay time of the HMPP device is prolonged. This prolonged photovoltage decay time and decreased leakage current in dark current density–voltage (J–V) curves (Figure S18) jointly reflect the suppressed non-radiative recombination [23, 58]. We also calculate the ideality factor of the HMPP device to be 1.44, smaller than that of control PSCs (1.75), further indicating the suppressed non-radiative recombination (Figure 3e). This result is also validated by the electrochemical impedance spectroscopy (EIS) spectra with the HMPP PSCs shows an increased recombination resistance from 1.9×10^5 to 2.3×10^5 Ω and a reduced series resistance (R) decreased from 18.84 to 11.15 Ω [58, 59] (Figure 3f). The above results jointly

16146840, 2026, 28, Downloaded from https://advanced.onlinelibrary.wiley.com/doi/10.1002/aenm.71112 by North China Electric Power University Beijing, Wiley Online Library on [05/09/2026]. See the Terms and Conditions (https://onlinelibrary.wiley.com/terms-and-conditions) on Wiley Online Library for rules of use; OA articles are governed by the applicable Creative Commons License

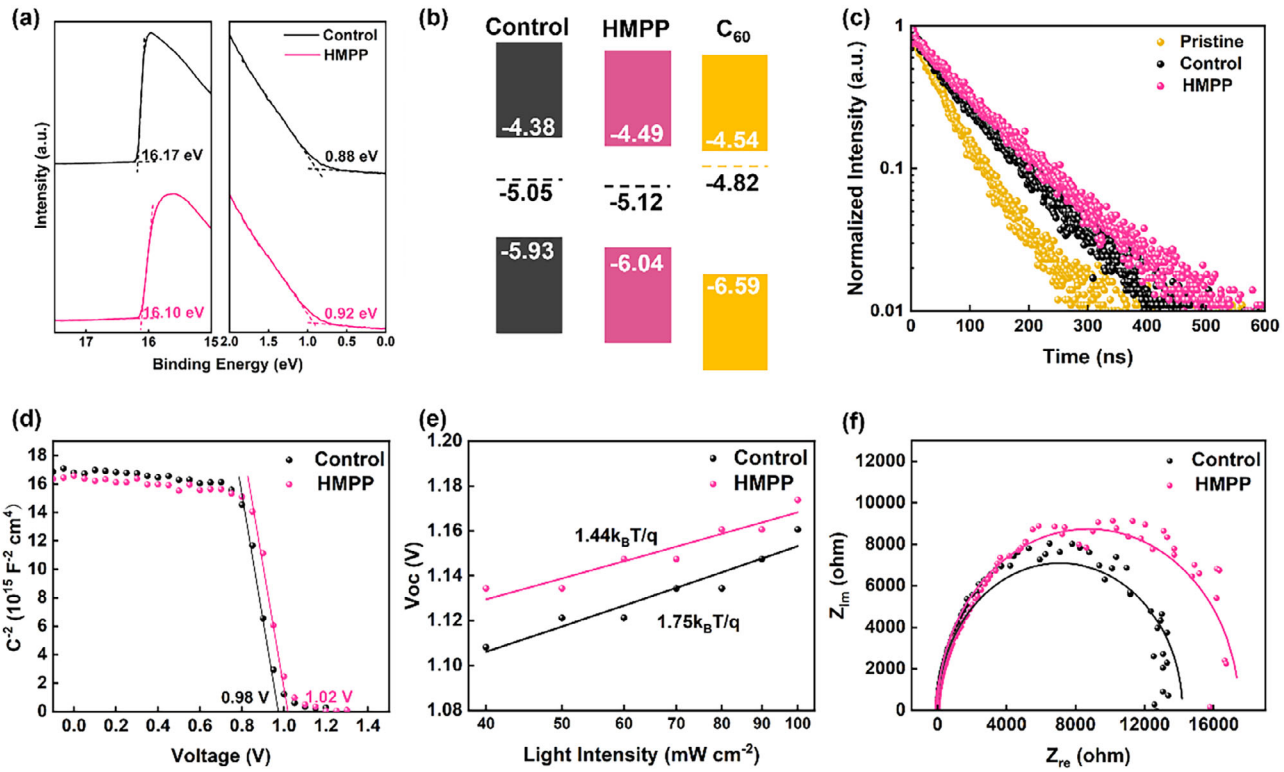


FIGURE 3 | Devise a physical property. (a) UPS spectra of control and HMPP perovskite films. (b) Energy level diagram from UPS measurement. (c) TRPL spectra of the pristine, control, and HMPP films deposited on fluorine-doped tin oxide (FTO) stacked with C_{60}. (d) Mott-Schottky plots of control and HMPP devices. (e) Light-intensity dependence on open-circuit voltage (V_{OC}) plots of control and HMPP devices. (f) Nyquist plots obtained from EIS measurements under dark conditions with a bias near open-circuit voltage (V_{OC}).

demonstrate that the PEA^+-AFBN pair can feasibly passivate the surface defects of the perovskite film and moderately optimize the interfacial energy level matching, which effectively reduces the interfacial carrier recombination.

To evaluate the contribution of PEA^+-AFBN passivation pair compared to single-passivation on the photovoltaic performance of PSCs, we fabricated devices with the architecture of FTO/hole transport layer (NiO_x with [4-(3,6-dimethyl-9H-carbazol-9-yl) butyl] phosphonic Acid)/perovskite/passivation layer/ETL (C_{60} with bathocuproine)/Ag. After experimental exploration, under a fixed initial concentration of PEACl (1 mg/mL), AFBN was added at concentrations of 0, 0.1, 0.2, and 0.3 mg/mL, respectively. The results indicate that an additional AFBN concentration of 0.2 mg/mL yields the most pronounced improvement in device performance. Statistical analysis of 15 devices confirmed that this ratio delivers both higher efficiency and better reproducibility, with an average PCE of 25.31%, fill factor (*FF*) of 84.02%, V_{OC} of 1.173 V, and short-circuit current density (J_{SC}) of 25.68 mA/cm^2 (Figure 4a). The *J*–*V* curves of champion PSCs are shown in Figure 4b. The control PSC achieved a PCE of 24.20%, with a V_{OC} of 1.16 V, a J_{SC} of 25.93 mA/cm^2, and an FF of 80.43%. As a comparison, the HMPP PSC obtained a PCE of 25.89%, with V_{OC}, J_{SC}, and FF values of 1.176 V, 25.78 mA/cm^2, and 85.37%, respectively. The forward and reverse-scan *J*–*V* curves of the champion HMPP-modified devices are displayed in Figure S19. To further investigate the origin of V_{OC} enhancement, we performed external electroluminescence quantum efficiency (EQE_{EL}) measurements to quantify the non-radiative voltage loss ($\triangle V_{OC,non\text{-}rad}$). When the injected current density is equal to the J_{SC}, the control device exhibits an EQE_{EL} of 4.97%, corresponding to a $\triangle V_{OC,non\text{-}rad}$ of 75.8 meV. Upon HMPP strategy, the EQE_{EL} increases to 7.42%, which translates to a reduced $\triangle V_{OC,non\text{-}rad}$ of 65.7 meV (Figure S20). This 10.1 meV reduction in non-radiative energy loss is in excellent agreement with the observed improvement in the steady-state V_{OC}.

To demonstrate the universality of the HMPP strategy toward analogous cations, we evaluated its efficacy using PEAI. As shown in Figure 4c, the addition of AFBN yielded a consistent improvement in PCE, mirroring the results obtained with PEACl. These results suggest that HMPP remains effective when the counter-anion is transitioned from Cl^- to I^-, demonstrating the potential versatility of this strategy within the phenethylammonium-based passivator family. The mechanism applicability of HMPP in ammonium systems was also investigated. We performed FTIR spectroscopy and ^1H NMR spectroscopy on HMPP systems incorporating $PDAI_2$ (common passivator in inverted structure) and CHEAI (common passivator in regular structure) to probe the intermolecular interactions (Figures S21 and S22). The results reveal that, regardless of the differences in cation structures, both PDA^{2+} and $CHEA^+$ are capable of forming analogous hydrogen bonds with AFBN via their $-NH_3^+$ groups, consistent with the PEACl system. Furthermore, the HMPP strategy was experimentally validated in both inverted p-i-n (with $PDAI_2$) and regular n-i-p

16146840, 2026, 28, Downloaded from https://advanced.onlinelibrary.wiley.com/doi/10.1002/aenm.71112 by North China Electric Power University Beijing, Wiley Online Library on [05/09/2026]. See the Terms and Conditions (https://onlinelibrary.wiley.com/terms-and-conditions) on Wiley Online Library for rules of use; OA articles are governed by the applicable Creative Commons License

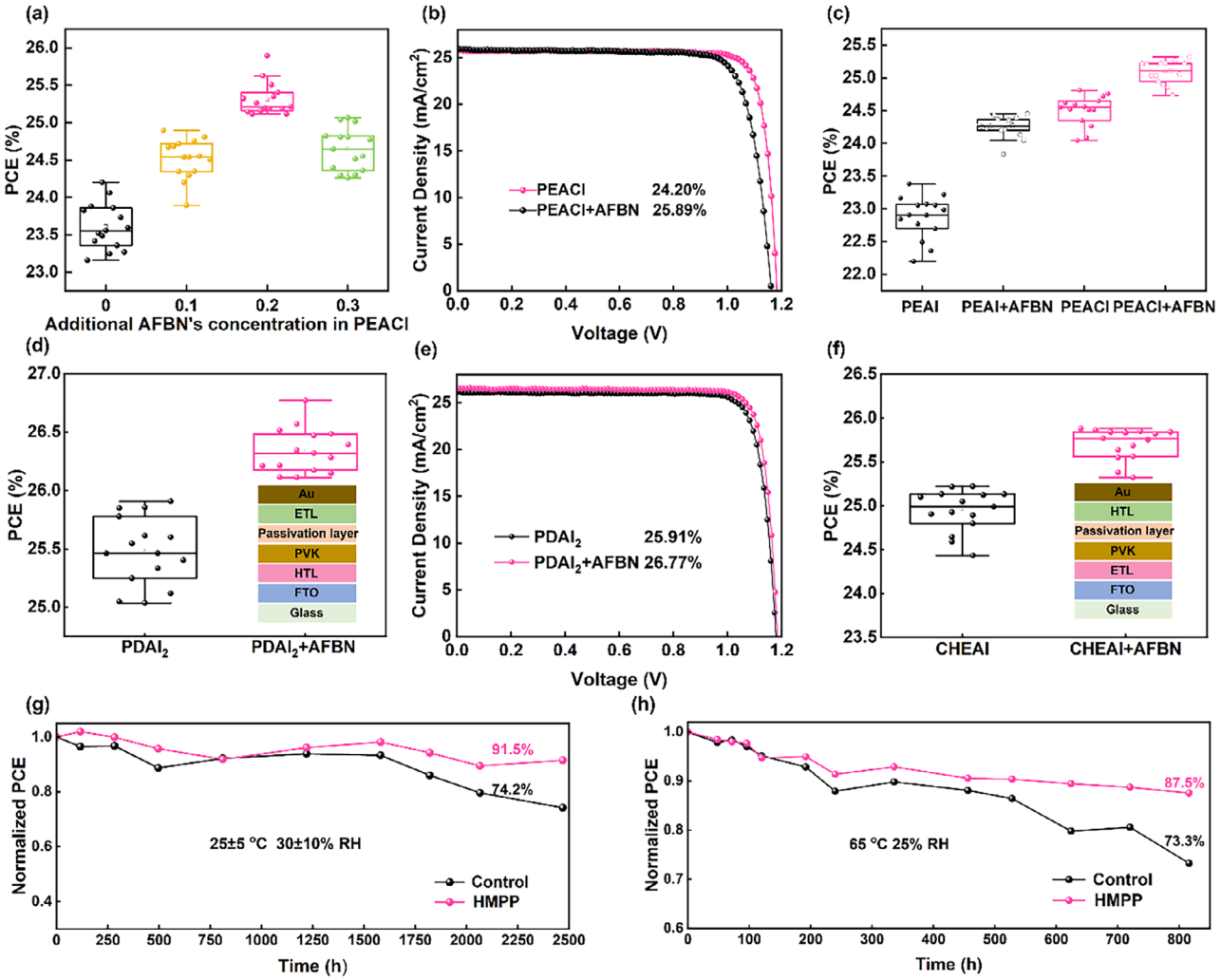


FIGURE 4 | Photovoltaic performance of PSCs. (a) PCE statistics of PEACl-based p-i-n devices modified by a set of concentrations of AFBN (15 devices for each set). (b) *J–V* curves of PEACl passivated device and corresponding HMPP-modified device. (c) PCE statistics of PEAI, PEAI-AFBN, PEACl, PEACl-AFBN-based devices (15 devices for each set). (d) PCE statistics of $PDAI_2$-based p-i-n devices before and after modification by HMPP (15 devices for each set). (e) *J–V* curves of devices of $PDAI_2$ passivated device and the corresponding HMPP-modified device. (f) PCE statistics of CHEAI-based device n-i-p devices before and after modification by HMPP (15 devices for each set). Normalized PCE decay curves of the unencapsulated control and HMPP devices exposed to (g) ambient environment with 25 ± 5°C, 30 ± 10% RH, and (h) 65°C, 25% RH.

(with CHEAI) perovskite devices. For each device architecture, 15 control devices and 15 HMPP devices were fabricated, and their photovoltaic performances were statistically compared. The average efficiencies of $PDAI_2$-based devices increased from 25.49% to 26.34% after incorporating AFBN (Figure 4d). Importantly, applying this strategy to the $PDAI_2$-based passivation system enabled the HMPP device to deliver a maximum PCE of 26.77%, featuring a V_{OC} of 1.189 V, a J_{SC} of 26.51 mA/cm^2, and a FF of 84.89%. Figure S23 illustrates the *J–V* curves recorded in both scanning directions. Whereas for the device with $PDAI_2$ alone, the highest efficiency reaches 25.91%, with a J_{SC} of 26.13 mA cm^{-2}, a V_{OC} of 1.174 V, and an FF of 84.46% (Figure 4e). The external quantum efficiency spectra (Figure S24) of the two groups show that the integrated current matches well with their respective short-circuit current densities. Furthermore, we incorporated AFBN with the CHEAI passivator, which is widely employed in n-i-p architectures to validate its functional versatility. The HMPP strategy led to a clear enhancement in device performance, with the average PCE of 15 devices increasing from 24.94% to 25.71% (Figure 4f). It can be observed that the advantage of AFBN also extends to the chain-like $PDAI_2$ molecule with dual ammonium groups and the cyclic ammonium salt CHEAI, and it remains operative across n–i–p and p–i–n configurations despite their intrinsically different perovskite surface chemistries, demonstrating the reliable universality.

Furthermore, the influence of the HMPP strategy on device stability with the passivator of PEACl is also explored. Under continuous irradiation for 300 s, the device sustained a stabilized efficiency above 26% without any detectable decay (Figure S25). By contrast, the control device stabilized at ~25% under the same 300 s illumination and exhibited noticeable degradation (Figure S26). The water contact angle of the perovskite film increased from 46.5° to 50.4° after HMPP treatment (Figure S27), indicating an enhanced surface hydrophobicity. This improvement suggests that the HMPP modification effectively creates a more moisture-resistant surface, which is beneficial for the long-term stability of the resulting devices. After nearly 2500 h of storage in air

16146840, 2026, 28, Downloaded from https://advanced.onlinelibrary.wiley.com/doi/10.1002/aenm.71112 by North China Electric Power University Beijing, Wiley Online Library on [05/09/2026]. See the Terms and Conditions (https://onlinelibrary.wiley.com/terms-and-conditions) on Wiley Online Library for rules of use; OA articles are governed by the applicable Creative Commons License

with 30% relative humidity without encapsulation, the HMPP devices were able to retain 91.5% of their initial efficiency, whereas the control counterparts degraded to 74.2% (Figure 4g). Moreover, under storage at a constant relative humidity of 25% and an elevated temperature of 65°C, the HMPP devices retained 87.5% of their initial efficiency after 800 h, whereas the control devices degraded to only 73.3% (Figure 4h; Tables S2 and S3). Devices modified with HMPP also exhibit improved operational stability after maximum power point (MPP) tracking under 1-sun illumination in N_2 glovebox (Figure S28). A direct comparison between continuous operational stability tests and long-term environmental storage tests demonstrates that the HMPP strategy enhances the damp-heat stability of the perovskite films by constructing a more uniform and compact passivation layer.

3 | Conclusion

In summary, we proposed a universal passivation strategy by constructing the hydrogen bond-mediated molecule-cation passivation pair (HMPP), achieving high-efficiency PSCs. The HMPP strategy enhances the passivation uniformity through dispersing the local aggregation of traditional ammonium salts and improves the passivation effectiveness through addressing multitype defects, which reduces the interfacial carrier recombination and promotes the interfacial carrier transport. As a result, the HMPP strategy boosts the efficiency of PSCs based on PEACl passivator from 24.20% to 25.89%. This strategy also shows a satisfying universality on different ammonium passivators. The HMPP-PSCs based on $PDAI_2$ passivator achieved an efficiency of 26.77%. The regular HMPP-PSCs based on CHEAI passivator achieved an efficiency of 25.88%. In addition, the unencapsulated HMPP-PSCs exhibited an enhanced long-term stability by maintaining ~91.5% and ~87.5% of their initial PCE after aging under ambient conditions for nearly 2500 h and 65°C for 800 h, respectively. Our systematic investigation into the homogeneity of composite passivators, combined with the proposed HMPP strategy, provides a reliable guideline for mitigating defect-mediated carrier recombination, thereby paving the way for breakthrough improvements in the photovoltaic performance of PSCs.

Acknowledgements

This work is supported partially by National Natural Science Foundation of China (Grant nos. 52232008, 52402254, 52072121), Beijing Natural Science Foundation (Z240024, 26JL001), 2022 Strategic Research Key Project of Science and Technology Commission of the Ministry of Education, Huaneng Group Headquarters Science and Technology Project (HNKJ20-H88), the Fundamental Research Funds for the Central Universities (2024JC005) and the NCEPU "Double First-Class" Program.

Conflicts of Interest

The authors declare no conflicts of interest.

Data Availability Statement

The data that support the findings of this study are available from the corresponding author upon reasonable request.

References

1. K. Artuk, D. Turkay, M. D. Mensi, et al., "A Universal Perovskite/C60 Interface Modification via Atomic Layer Deposited Aluminum Oxide for Perovskite Solar Cells and Perovskite–Silicon Tandems," *Advanced Materials* 36 (2024): 2311745.

2. B. Chen, P. N. Rudd, S. Yang, Y. Yuan, and J. Huang, "Imperfections and Their Passivation in Halide Perovskite Solar Cells," *Chemical Society Reviews* 48 (2019): 3842–3867, https://doi.org/10.1039/C8CS00853A.

3. P. Chen, Y. Xiao, S. Li, et al., "The Promise and Challenges of Inverted Perovskite Solar Cells," *Chemical Reviews* 124 (2024): 10623–10700, https://doi.org/10.1021/acs.chemrev.4c00073.

4. Q. Jiang, Y. Zhao, X. Zhang, et al., "Author Correction: Surface Passivation of Perovskite Film for Efficient Solar Cells," *Nature Photonics* 13 (2019): 500, https://doi.org/10.1038/s41566-019-0462-y.

5. C. Liu, Y.-B. Cheng, and Z. Ge, "Understanding of Perovskite Crystal Growth and Film Formation in Scalable Deposition Processes," *Chemical Society Reviews* 49 (2020): 1653–1687, https://doi.org/10.1039/C9CS00711C.

6. J. Liu, M. De Bastiani, E. Aydin, et al., "Efficient and Stable Perovskite-silicon Tandem Solar Cells through Contact Displacement by MgF X," *Science* 377 (2022): 302–306, https://doi.org/10.1126/science.abn8910.

7. S. Pratap, F. Babbe, N. S. Barchi, et al., "Out-of-equilibrium Processes in Crystallization of Organic-inorganic Perovskites during Spin Coating," *Nature Communications* 12 (2021): 5624, https://doi.org/10.1038/s41467-021-25898-5.

8. A. R. B. Mohd Yusoff, M. Vasilopoulou, D. G. Georgiadou, L. C. Palilis, A. Abate, and M. K. Nazeeruddin, "Passivation and Process Engineering Approaches of Halide Perovskite Films for High Efficiency and Stability Perovskite Solar Cells," *Energy & Environmental Science* 14 (2021): 2906–2953, https://doi.org/10.1039/D1EE00062D.

9. S. Wang, A. Wang, X. Deng, et al., "Lewis Acid/Base Approach for Efficacious Defect Passivation in Perovskite Solar Cells," *Journal of Materials Chemistry A* 8 (2020): 12201–12225, https://doi.org/10.1039/D0TA03957H.

10. M. Zhang, Y. Guo, M. Wang, et al., "Surface Co-passivation for 1.7 eV Wide-bandgap Perovskite Solar Cells with Minimal Voltage Loss to Achieve over 23% Efficiency," *Science Bulletin* 71 (2025): 345–357.

11. Z.-R. Lan, Y.-D. Wang, J.-Y. Shao, et al., "Surface Passivation with Diaminopropane Dihydroiodide for p-i-n Perovskite Solar Cells with over 25% Efficiency," *Advanced Functional Materials* 34 (2024): 2312426, https://doi.org/10.1002/adfm.202312426.

12. X. Zhang, Y. Luo, X. Wang, et al., "Locking Surface Dimensionality for Endurable Interface in Perovskite Photovoltaics," *Carbon Energy* 7 (2025): 718, https://doi.org/10.1002/cey2.718.

13. A. Maqsood, Y. Li, J. Meng, et al., "Organic Halide PEACl for Surface Passivation and Defects Suppression in Perovskite Solar Cells," *ACS Applied Energy Materials* 4 (2021): 12411–12420, https://doi.org/10.1021/acsaem.1c02210.

14. W.-Q. Wu, P. N. Rudd, Q. Wang, Z. Yang, and J. Huang, "Blading Phase-Pure Formamidinium-Alloyed Perovskites for High-Efficiency Solar Cells with Low Photovoltage Deficit and Improved Stability," *Advanced Materials* 32 (2020): 2000995, https://doi.org/10.1002/adma.202000995.

15. Y. Yu, M. Xu, R. Liu, H. Ren, and J. Chen, "Molecular Cation Passivation and Bromine Vacancy Supplement Strategy for Efficient Wide-Bandgap Perovskite Solar Cells," *Chemical Engineering Journal* 507 (2025): 160339, https://doi.org/10.1016/j.cej.2025.160339.

16. T.-H. Han, S. Tan, J. Xue, L. Meng, J.-W. Lee, and Y. Yang, "Interface and Defect Engineering for Metal Halide Perovskite Optoelectronic Devices," *Advanced Materials* 31 (2019): 1803515, https://doi.org/10.1002/adma.201803515.

17. D. B. Khadka, Y. Shirai, M. Yanagida, et al., "Defect Passivation in Methylammonium/Bromine Free Inverted Perovskite Solar Cells

16146840, 2026, 28, Downloaded from https://advanced.onlinelibrary.wiley.com/doi/10.1002/aenm.71112 by North China Electric Power University Beijing, Wiley Online Library on [05/09/2026]. See the Terms and Conditions (https://onlinelibrary.wiley.com/terms-and-conditions) on Wiley Online Library for rules of use; OA articles are governed by the applicable Creative Commons License

Using Charge-Modulated Molecular Bonding," *Nature Communications* 15 (2024): 882, https://doi.org/10.1038/s41467-024-45228-9.

18. Z. Liu, K. Meng, X. Wang, et al., "In Situ Observation of Vapor-Assisted 2D–3D Heterostructure Formation for Stable and Efficient Perovskite Solar Cells," *Nano Letters* 20 (2020): 1296–1304, https://doi.org/10.1021/acs.nanolett.9b04759.

19. S. Teale, M. Degani, B. Chen, E. H. Sargent, and G. Grancini, "Molecular Cation and Low-Dimensional Perovskite Surface Passivation in Perovskite Solar Cells," *Nature Energy* 9 (2024): 779–792, https://doi.org/10.1038/s41560-024-01529-3.

20. S. D. Stranks, "Multimodal Microscopy Characterization of Halide Perovskite Semiconductors: Revealing a New World (dis) Order," *Matter* 4 (2021): 3852–3866.

21. H. Chen, C. Liu, J. Xu, et al., "Improved Charge Extraction in Inverted Perovskite Solar Cells with Dual-site-binding Ligands," *Science* 384 (2024): 189–193, https://doi.org/10.1126/science.adm9474.

22. C. Liu, Y. Yang, H. Chen, et al., "Bimolecularly Passivated Interface Enables Efficient and Stable Inverted Perovskite Solar Cells," *Science* 382 (2023): 810–815, https://doi.org/10.1126/science.adk1633.

23. Q. Cai, Q. Tan, J. He, et al., "Enhancing Electron Transport for Efficiency-Recorded HTL-Free Inverted Perovskite Solar Cells by Molecular Complementary Passivation," *Joule* 9 (2025): 101880.

24. H. Zhao, J. Ding, X. Liu, et al., "Intermolecular Interaction Induced Synergistic Uniform Passivation of Grain Boundary Multiple Defects Enables High-Performance Inverted Perovskite Solar Cells," *Advanced Functional Materials* (2025): 2504424, https://doi.org/10.1002/adfm.202504424.

25. X. Jiang, J. Zhang, X. Liu, Z. Wang, X. Guo, and C. Li, "Deeper Insight into the Role of Organic Ammonium Cations in Reducing Surface Defects of the Perovskite Film," *Angewandte Chemie International Edition* 61 (2022): 202115663, https://doi.org/10.1002/anie.202115663.

26. E. A. Alharbi, A. Y. Alyamani, D. J. Kubicki, et al., "Atomic-Level Passivation Mechanism of Ammonium Salts Enabling Highly Efficient Perovskite Solar Cells," *Nature Communications* 10 (2019): 3008, https://doi.org/10.1038/s41467-019-10985-5.

27. O. I. Gnezdilov, O. N. Antzutkin, R. Gimatdinov, and A. Filippov, "Temperature Dependence of 1H NMR Chemical Shifts and Diffusivity of Confined Ethylammonium Nitrate Ionic Liquid," *Magnetic Resonance Imaging* 74 (2020): 84–89, https://doi.org/10.1016/j.mri.2020.09.012.

28. A. Bagno, E. Menna, G. Scorrano, and S. Zerbinati, "NMR Properties (chemical shift and relaxation rate) of Acceptor and Hydrogen Bridge Nuclei in Hydrogen-Bonded Complexes," *Magnetic Resonance in Chemistry* 39 (2001): S59–S66.

29. S. Kajal, J. Jeong, J. Seo, et al., "Coordination Modulated Passivation for Stable Organic-Inorganic Perovskite Solar Cells," *Chemical Engineering Journal* 451 (2023): 138740, https://doi.org/10.1016/j.cej.2022.138740.

30. E. Kose and M. S. Vanli, "Theoretical, Experimental, and Molecular Docking Investigation of Comparative Structural, Spectroscopic, and Electronic Features of 2-, 3-, and 4-aminobenzylamine Molecules," *Journal of Molecular Structure* 1364 (2026): 145836, https://doi.org/10.1016/j.molstruc.2026.145836.

31. M. J. Mphahlele, M. M. Maluleka, L. Rhyman, P. Ramasami, and R. M. Mampa, "Spectroscopic, DFT, and XRD Studies of Hydrogen Bonds in N-Unsubstituted 2-Aminobenzamides," *Molecules* 22 (2017): 83, https://doi.org/10.3390/molecules22010083.

32. R. M. Silverstein, F. X. Webster, and D. J. Kiemle, *Spectrometric Identification of Organic Compounds* (John Wiley & Sons, 2014).

33. M. Safferthal, K. Greis, R. Chang, et al., "Cryogenic Infrared Spectroscopy Reveals Remarkably Short $NH^+ \cdots F$ Hydrogen Bonds in Fluorinated Phenylalanines," *Physical Chemistry Chemical Physics* 25 (2023): 24783–24788, https://doi.org/10.1039/D3CP03776B.

34. G. Socrates, *Infrared and Raman Characteristic Group Frequencies: Tables and Charts* (John Wiley & Sons, 2001).

35. K. Feng, G. Wang, Q. Lian, et al., "Non-Fullerene Electron-Transporting Materials for High-Performance and Stable Perovskite Solar Cells," *Nature Materials* 24 (2025): 770–777, https://doi.org/10.1038/s41563-025-02163-4.

36. Y. Li, L. Dong, Y. Cai, et al., "Meticulous Design of High-Polarity Interface Material for $FACsPbI_3$ Perovskite Solar Cells with Efficiency of 26.47%," *Angewandte Chemie International Edition* 64 (2025): 202504902.

37. L. Liu, Y. Ma, Y. Wang, et al., "Hole-Transport Management Enables 23%-Efficient and Stable Inverted Perovskite Solar Cells with 84% Fill Factor," *Nano-Micro Letters* 15 (2023): 117, https://doi.org/10.1007/s40820-023-01088-4.

38. W.-T. Wang, P. Holzhey, N. Zhou, et al., "Water- and Heat-Activated Dynamic Passivation for Perovskite Photovoltaics," *Nature* 632 (2024): 294–300, https://doi.org/10.1038/s41586-024-07705-5.

39. Y. Zhang, Y. Liu, Z. Zhao, et al., "Reduction of Nonradiative Recombination at Perovskite/C_{60} Interface in Inverted Perovskite Solar Cells," *Advanced Materials* 37 (2025): 2500501, https://doi.org/10.1002/adma.202500501.

40. X. Jia, K. Zhang, X. Gao, et al., "Defect Passivation and Crystallization Modulation in Methylammonium-free Wide-bandgap Perovskites for all-perovskite Tandem Solar Cells," *Science Advances* 11 (2025): adv4501, https://doi.org/10.1126/sciadv.adv4501.

41. D. Wang, Y. Li, W. Li, et al., "Tailoring Dual-Site Defect Passivation Molecules to Minimize Buried Interface Energy Loss for Highly Efficient and Stable Perovskite Solar Cells," *Angewandte Chemie* 137 (2025): 202509529.

42. G. Xiong, Y. Fu, X. Ling, et al., "Interface Tailoring by Multifunctional Metal–Organic Salts Enables Efficient Perovskite Solar Cells with a Fill Factor over 86%," *Advanced Functional Materials* 36 (2025): 15859.

43. Y. Cao, L. Yang, N. Yan, et al., "Buried Interface Modification for High Performance and Stable Perovskite Solar Cells," *Energy & Environmental Science* 18 (2025): 3659–3667, https://doi.org/10.1039/D4EE05466K.

44. J. Jiang, Z. Xia, M. Shi, et al., "Efficient Red Perovskite LEDs with Iodine Management via Volatile Additive I 2," *Advanced Materials* 37 (2025): 2503699, https://doi.org/10.1002/adma.202503699.

45. Y. Jiang, X. Sun, T. Liu, et al., "Surface Reaction Induced Compressive Strain for Stable Inorganic Perovskite Solar Cells," *Angewandte Chemie International Edition* 63 (2024): 202410721, https://doi.org/10.1002/anie.202410721.

46. D. Liu, J. Bi, W. Xu, et al., "Strain Relaxation in Halide Perovskites via 2D/3D Perovskite Heterojunction Formation," *Science Advances* 11 (2025): adu3459, https://doi.org/10.1126/sciadv.adu3459.

47. F. Pei, S. Lin, Z. Zhang, et al., "Inhibiting Defect Passivation Failure in Perovskite for Perovskite/Cu(In,Ga)Se_2 Monolithic Tandem Solar Cells with Certified Efficiency 27.35%," *Nature Energy* 10 (2025): 824–835.

48. J. Cheng, H. Cao, S. Zhang, et al., "Enhanced Electric Field Minimizing Quasi-Fermi Level Splitting Deficit for High-Performance Tin-Lead Perovskite Solar Cells," *Advanced Materials* 36 (2024): 2410298, https://doi.org/10.1002/adma.202410298.

49. F. Gao, H. Li, B. Jiao, et al., "Perovskite Facet Heterojunction Solar Cells," *Joule* 9 (2025): 101787.

50. Y. Guo, F. Yao, Y. Zhang, et al., "A Universal Surface Fixed Charge Reconstruction Strategy to Minimize Contact Loss in Wide Bandgap Perovskite Photovoltaics," *Energy & Environmental Science* 18 (2025): 4916–4924, https://doi.org/10.1039/D4EE05855K.

51. J. Wang, L. Zheng, H.-B. Kim, et al., "Dipolar Carbazole Ammonium for Broadened Electric Field Distribution in High-Performance Perovskite Solar Cells," *Journal of the American Chemical Society* 147 (2025): 8663–8671, https://doi.org/10.1021/jacs.4c18074.

16146840, 2026, 28, Downloaded from https://advanced.onlinelibrary.wiley.com/doi/10.1002/aenm.71112 by North China Electric Power University Beijing, Wiley Online Library on [05/09/2026]. See the Terms and Conditions (https://onlinelibrary.wiley.com/terms-and-conditions) on Wiley Online Library for rules of use; OA articles are governed by the applicable Creative Commons License

52. Z. Zhang, J. Ding, H. Liu, et al., "Immobilizing Lead and Healing Surface Defects via Perfluorinated Tertiary Amine Molecules Enables High-Performance Sustainable Inverted Perovskite Solar Cells," *Advanced Materials* 37 (2025): 2508126, https://doi.org/10.1002/adma.202508126.

53. J. Xue, R. Wang, X. Chen, et al., "Reconfiguring the Band-edge States of Photovoltaic Perovskites by Conjugated Organic Cations," *Science* 371 (2021): 636–640, https://doi.org/10.1126/science.abd4860.

54. Y. Cheng, H. Wan, E. H. Sargent, and D. Ma, "Reduced-Dimensional Perovskites: Quantum Well Thickness Distribution and Optoelectronic Properties," *Advanced Materials* 37 (2025): 2410633, https://doi.org/10.1002/adma.202410633.

55. A. Farag, T. Feeney, I. M. Hossain, et al., "Evaporated Self-Assembled Monolayer Hole Transport Layers: Lossless Interfaces in p-i-n Perovskite Solar Cells," *Advanced Energy Materials* 13 (2023): 2203982, https://doi.org/10.1002/aenm.202203982.

56. Y. Wang, Y. Feng, H. Yang, et al., "Covalent Tridentate Molecule Anchoring Enhances Nickel Oxide for Efficient Perovskite Solar Cells," *Advanced Materials* 37 (2025): 07730, https://doi.org/10.1002/adma.202507730.

57. S. Yuan, C. Ge, T. Zhang, et al., "Conjugated Bisphosphonic Acid Self-assembled Monolayers for Efficient and Stable Inverted Perovskite Solar Cells," *Journal of the American Chemical Society* 147 (2025): 24662–24671.

58. Y. Li, X. He, R. Zhu, et al., "Enhanced Corrosion Resistance of Ag Electrode through Ionized 2-Mercaptobenzothiazole in Inverted Perovskite Solar Cells," *Advanced Functional Materials* 35 (2025): 2413245, https://doi.org/10.1002/adfm.202413245.

59. C. Zhou, W. Wang, H. Wu, et al., "Bimolecular Amine Vapor Passivation for Efficient Perovskite Solar Cells Based on Blade-coated $FAPbI_3$," *Energy & Environmental Science* 18 (2025): 9149–9157.

Supporting Information

Additional supporting information can be found online in the Supporting Information section.

Supporting File: aenm71112-sup-0001-SuppMat.docx.

16146840, 2026, 28, Downloaded from https://advanced.onlinelibrary.wiley.com/doi/10.1002/aenm.71112 by North China Electric Power University Beijing, Wiley Online Library on [05/09/2026]. See the Terms and Conditions (https://onlinelibrary.wiley.com/terms-and-conditions) on Wiley Online Library for rules of use; OA articles are governed by the applicable Creative Commons License